Construction of MnO_2-Mn_3O_4 heterostructures to facilitate high-performance aqueous magnesium ion energy storage

Xueli Chen[a,b], Lu Han[a,*], Guangzhen Zhao[a], Litao Zhao[a], Guoliang Gao[a], Lianghao Yu[a], Yanjiang Li[a], Xiuyang Shan[a], Junfeng Li[c], Xinjuan Liu [d], Guang Zhu [a, b,*]

[a] Key Laboratory of Spin Electron and Nanomaterials of Anhui Higher Education Institutes, Suzhou University, Suzhou 234000, PR China

[b] School of Materials Science and Engineering, Anhui Polytechnic University, Wuhu 241000, PR China

[c] College of Logistics Engineering, Shanghai Maritime University, Shanghai 201306, PR China

[d] School of Materials and Chemistry, University of Shanghai for Science and Technology, Shanghai 200093, P.R. China

** Corresponding author: Lu Han (982563331@qq.com);*

Guang Zhu (guangzhu@ahszu.edu.cn)

Materials Characterization

Field emission scanning electron microscopy (SEM, Hitachi, S-4800) with energy dispersive spectrometer (EDS, Bruker Quantax-400) and transmission electron microscope (TEM, JEM-2100F, JEOL) were used to examine the morphology, structure, and element distribution of the materials. Measurements of the sample's microstructure was made using an X-ray diffractometer (XRD, Rigaku Smart Lab, TM 9kW, Cu-K, = 1.5418A, 30 kV, 25 mA, scanning range 5-90°). Measurements of the sample's specific surface area and pore distribution were made using a physical adsorption instrument (Micrometric, ASAP2020). In order to suit the XPS test results, XPS Peak 4.1 software was used to assess the material element composition and valence states using X-ray photoelectron spectroscopy (XPS, Esca lab 250Xi).

Electrochemical Measurements.

The electrochemical characteristics of the samples were measured using an apparatus with three electrodes. The working electrodes were prepared by coating a homogenous slurry of active material (AC, MnO_2, MnO_2-Mn_3O_4, Mn_3O_4 power), carbon black (Super-P) and polyvinylidene fluoride (adhesive agent) in N-methyl pyrrolidone solvent with a weight ratio of 80: 10: 10 onto graphite substrates, and then dried at 60 °C for 24 h in a constant temperature oven. A saturated calomel electrode served as the reference electrode, and a Pt sheet served as the counter electrode. Typically, each working electrode has an exposed area of 1 × 1 cm^2 and an active material mass loading of 1 mg. As the electrolyte solution, we utilized 1.0 M $MgSO_4$ solution. An electrochemical workstation was used to measure cyclic voltammetry (CV), galvanostatic charge-discharge curves (GCD), and electrochemical impedance spectroscopy (EIS) (Autolab PGSTA302N). The voltage range for CV is -0.5 to 1.2 V (versus Hg/HgO), and the scan rates range from 2 to 10 mV s^{-1}. The voltage range for GCD is -0.5 to 1.2 V (versus Hg/HgO), and the current density ranges from 0.2 to 5 A g^{-1}. The frequency range used for the electrochemical impedance spectroscopy was 1 MHz to 0.1 Hz. A two-electrode system (MHS) was assembled using the AC electrode as the anode and the MnO_2-Mn_3O_4 electrode as the cathode in a 1 M $MgSO_4$ aqueous electrolyte. Similarly, the electrochemical performance of MHS was tested using an

electrochemical workstation (Autolab PGSTA302N). The cycling stability measurement of aqueous magnesium-ion hybrid supercapacitors (MHS) was carried out on a LAND battery-testing instrument with a current density at 10 A g^{-1} for 5000 cycles. The two-electrode test employed the principle of excess negative mass for electrode matching. A single negative electrode was coated with approximately 9 mg of active material, while a single positive electrode was coated with approximately 3 mg of active material. This ensured maximum capacity of the positive material. The active substance mass was used to compute all working current densities.

Related calculations. For the three-electrode and two-electrode systems, the specific capacitance (C_{F1}, F g^{-1}; C_{F2}, F g^{-1}) was calculated from the GCD curves according to the following equation[1, 2]:

$$C_{F1} = \frac{I \times \Delta t}{m \times \Delta V}$$

$$C_{F2} = \frac{I \times \Delta t}{m \times \Delta V}$$

where I, ΔV, m and t refer to the current (A), potential window (V), mass of active material (g) and discharge time (s), respectively.

For the two-electrode system, the energy density (E, Wh Kg^{-1}) and power density (P, W Kg^{-1}) were calculated according to the following equations[3, 4]:

$$E = \frac{C_F \times \Delta V^2}{2 \times 3.6}$$

$$P = \frac{3600 \times E}{\Delta t}$$

where C_F, ΔV, and Δt refer to the specific capacitance (F g^{-1}), potential window (V), and discharge time (s), respectively.

The ratio of diffusion and capacitance contributions in the capacity contribution is calculated as follows based on the ratio of diffusion-controlled and capacitance-controlled currents[5]:

$$i = k_1 v + k_2 v^{1/2}$$

k_1 and k_2 are fitting constants, vary with the scan rate of ν (mV s^{-1}), $k_1\nu$ being the faster capacitance control current and $k_2\nu^{1/2}$ being the slow diffusion control current.

The preparation of samples.

4 mmol $KMnO_4$ and 6 mmol $MnSO_4 \cdot H_2O$ were dissolved in 40 mL of DI, respectively. Then, the above two were mixed and stirred magnetically at room temperature for 30 min, and the mixed solution was transferred to a 100 ml polytetrafluoroethylene autoclave and kept at 140 °C for 6 h. The sample obtained by washing and drying is the precursor, and was denoted as MnO_2. The MnO_2 was transferred to a tube furnace and heated at 800 °C for 2 h under N_2 atmosphere at a rate of 2 °C min^{-1}. After natural cooling to room temperature, the sample was taken out and the MnO_2-Mn_3O_4 was obtained. Samples obtained under the same conditions at 1000 °C were Mn_3O_4.

M1:

$$xMg^{2+} + Mn_3O_4 + 2xe^- \underset{\text{Charge}}{\overset{\text{Discharge}}{\rightleftharpoons}} Mg_xMn_3O_4$$ **($Mn^{3+} \leftrightarrow Mn^{2+}$, Pseudo and EDLC)**

M2:

$$MnO_2 \underset{\text{Charge}}{\overset{\text{Discharge}}{\rightleftharpoons}} MnO_2$$ **($Mn^{4+} \leftrightarrow Mn^{4+}$, EDLC)**

Table S1 Mn and O species content (at%) of MnO_2, MnO_2-Mn_3O_4 and Mn_3O_4 based on XPS results.

Sample	Mn^{2+}	Mn^{3+}	Mn^{4+}	$O_{Mn-O-Mn}$	O_{Mn-OH}	O_{H-O-H}
MnO_2	-	-	100%	44.0%	35.2%	20.8%
MnO_2- Mn_3O_4	26.7%	36.5%	36.8%	55.8%	36.0%	8.2%
Mn_3O_4	44.86%	55.14%	-	64.1%	19.6%	16.3%

Table S2 Specific capacitance at varied current densities of MnO_2, MnO_2-Mn_3O_4 and Mn_3O_4.

Sample	0.5 A g^{-1}	1.0 A g^{-1}	2.0 A g^{-1}	3.0 A g^{-1}	5.0 A g^{-1}
MnO_2	132.1	108.8	76.4	55.6	32.4
MnO_2- Mn_3O_4	333.5	313.5	277.6	254.1	211.8
Mn_3O_4	155.0	123.5	78.8	52.9	29.4

Table S3 Performance comparison of MnO_2-Mn_3O_4 with other Mn-based materials in aqueous magnesium ion energy storage.

Anode	Cathode	Electrolyte	Energy density (W h kg^{-1})	Power density (W kg^{-1})	Cycling	Ref.
AC	K-MnO_2	1.0 M $MgSO_4$	85.2	360	96.7%, 20000 cycles	[5]
AC	Co-MnO_2	1.0 M $MgSO_4$	79.6	360	94.8%, 15000 cycles	[6]
AC	Mg-OMS-2/Graphene	0.5 M Mg $(NO_3)_2$	46.9	-	75.7%, 300 cycles	[7]
AC	β-MnO_2	1.0 M $MgSO_4$	60.8	180	74.1%, 3500 cycles	[8]
AC	δ-MnO_2	4.0 M Mg $(ClO_4)_2$	103.9	3680	96.5%, 1000 cycles	[9]
PCS	CMO/G-N	1.0 M Mg $(ClO_4)_2$	61.0	123	87%, 10000 cycles	[10]
AC	δ-MnO_2	4 M Mg $(ClO_4)_2$-PAAm	59.6	3450	96.7%, 1000 cycles	[11]
α-Fe_2O_3	β-MnO_2	1.0 M $MgSO_4$	82.1	6153	96.2%, 5000 cycles	[12]
AC	Mn_3O_4	2.0 M $MgSO_4$	20.2	125	80%, 6000 cycles	[13]
AC	K- MnO_2/HMC	1.0 M $MgSO_4$	111.1	505	97.3%, 5000 cycles	[14]
AC	**MnO_2-Mn_3O_4**	**1.0 M $MgSO_4$**	**185.6**	**1299.9**	**98.5%, 5000 cycles**	**This Work**

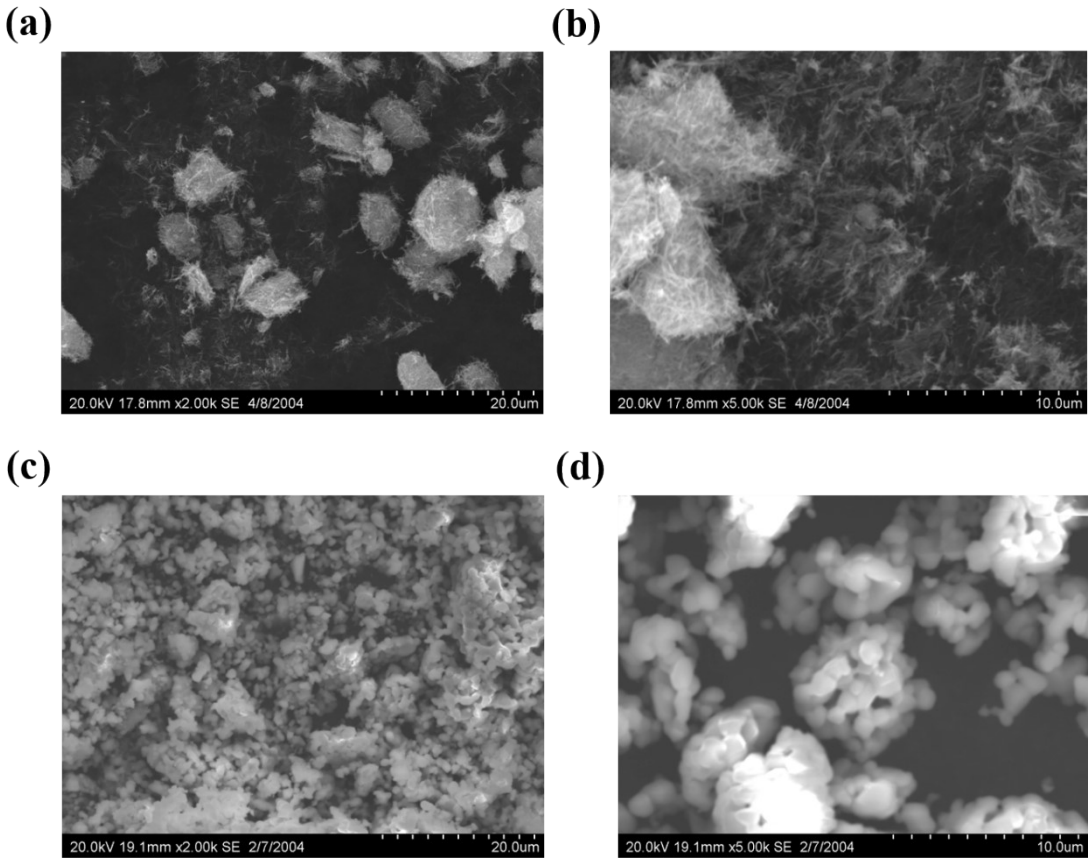

Fig.S1 SEM of MnO_2 (a, b) and Mn_3O_4 (c, d).

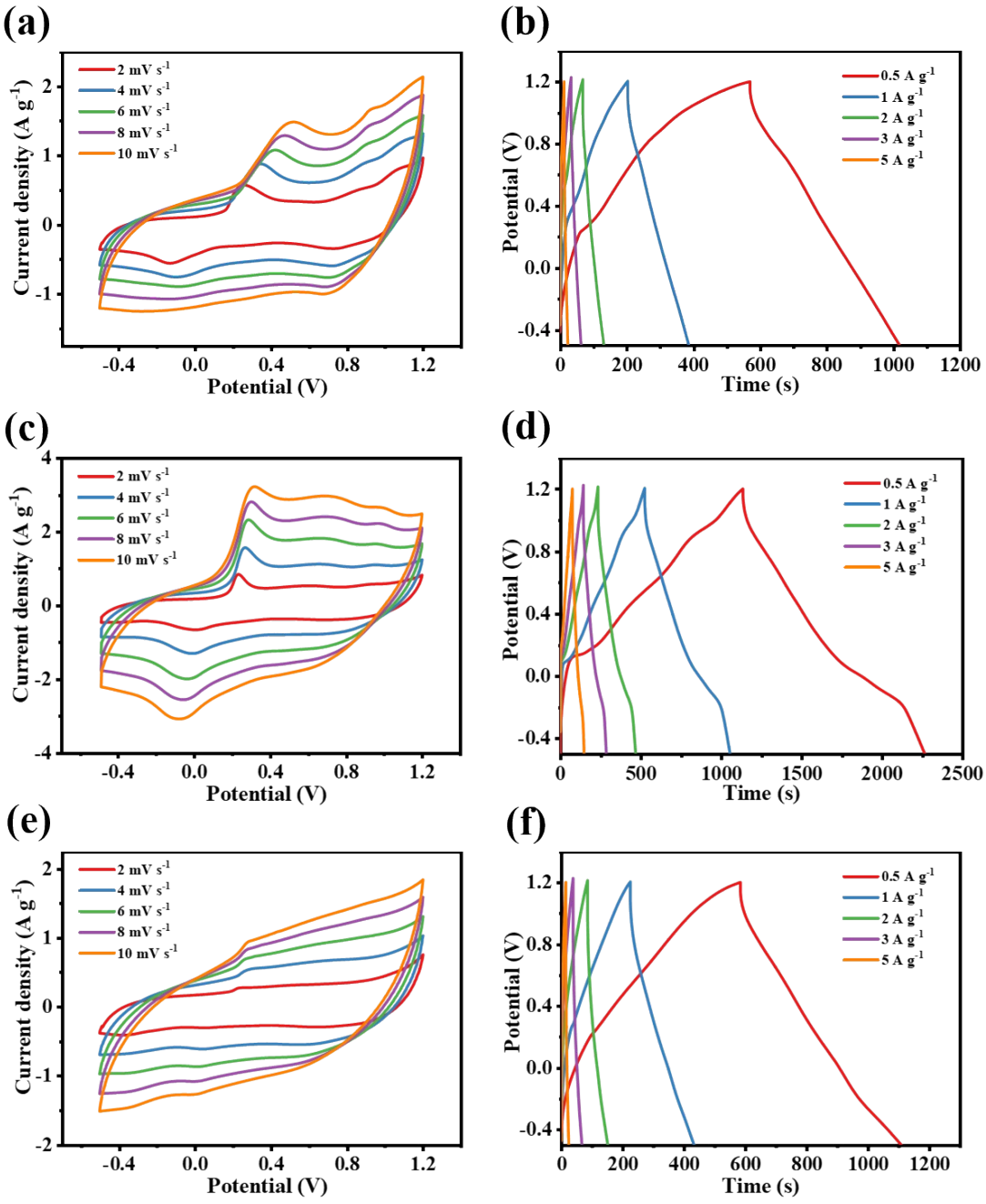

Fig.S2 CV curves at varied scan rates and GCD curves at varied current density of MnO_2 (a, b), MnO_2-Mn_3O_4 (c, d) and Mn_3O_4 (e, f).

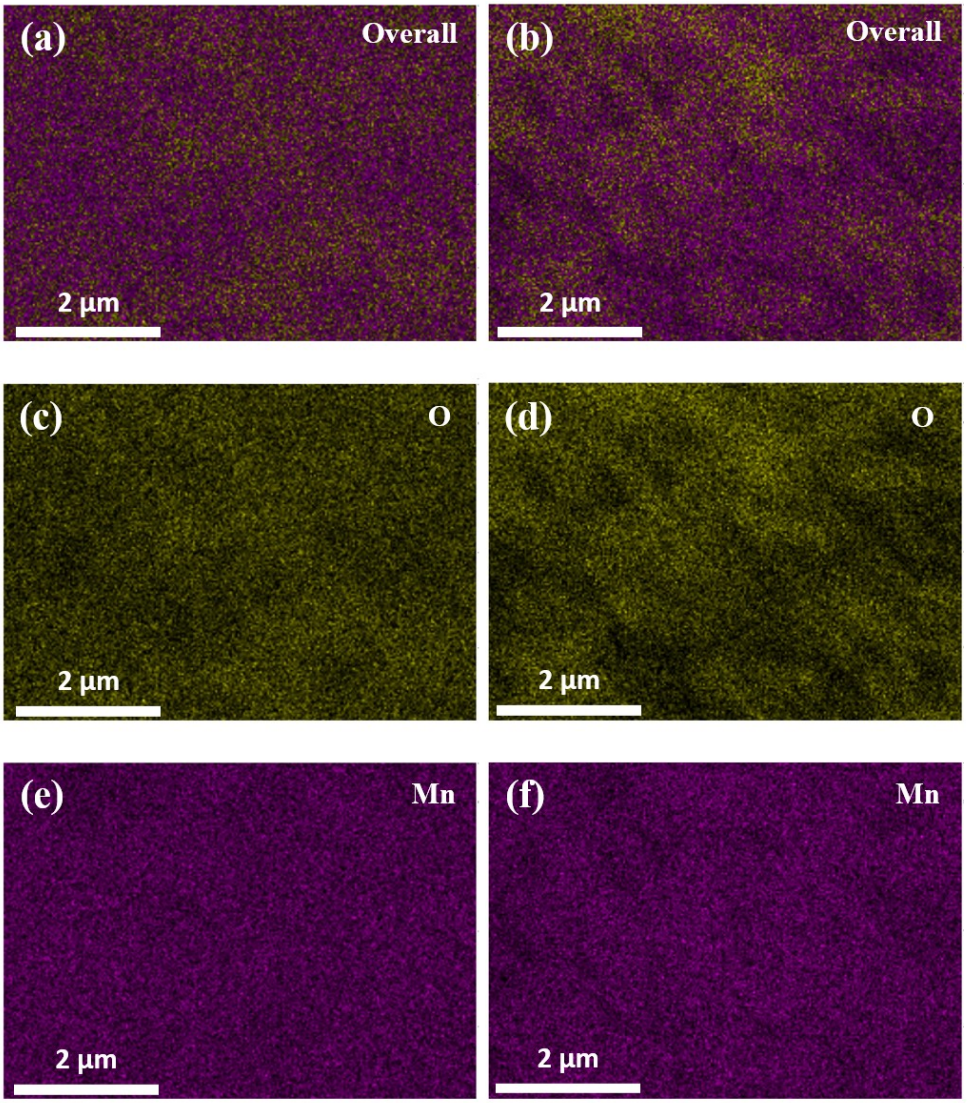

Fig.S3 EDS mapping of MnO_2 (a, c and e) and MnO_2-Mn_3O_4 (b, d and f).

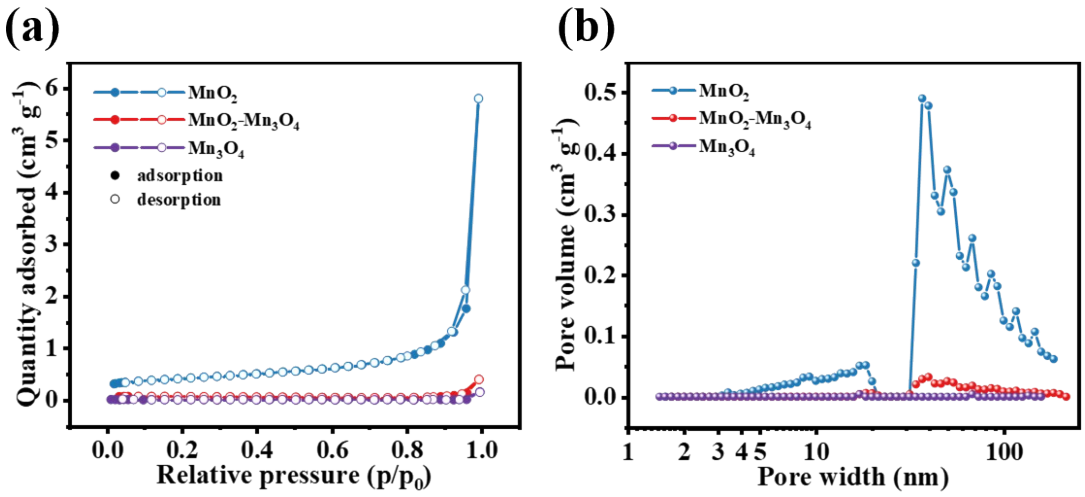

Fig.S4 (a) N_2 adsorption/desorption isotherms and (b) pore size distribution of the MnO_2, MnO_2-Mn_3O_4 and Mn_3O_4.

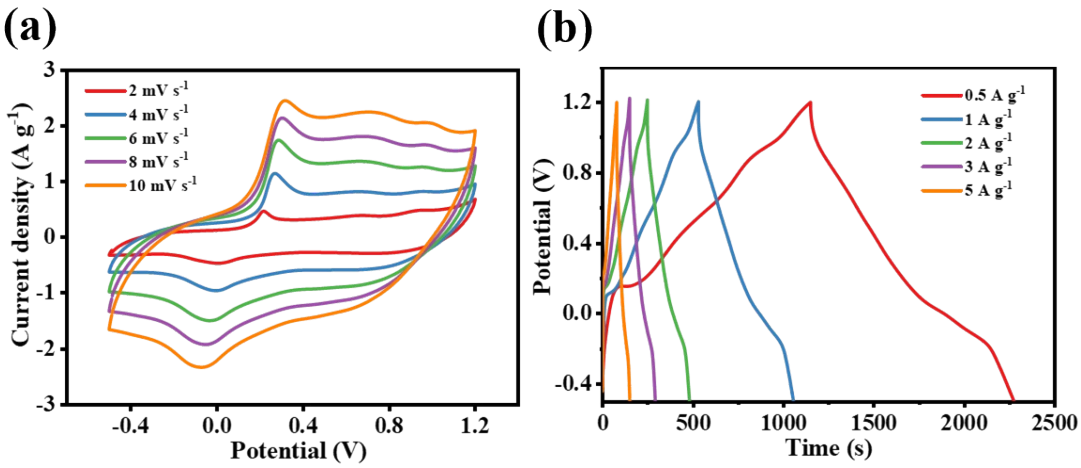

Fig.S5 Repeat experiments CV and GCD for MnO_2-Mn_3O_4 samples.

Reference

[1] L. Xu, D. Zhu, W. Zhou, F. Jiang, Y. Wu, Y. Cai, H. Kang, J. Xu, One-step hydrothermal synthesis of N-doped graphene/poly5-hydroxyindole composite materials for supercapacitor with ultra-long cycle stability and ultra-high energy storage performance. Journal of Energy Storage, 43 (2021) 103303.

[2] J. Zhang, L. Zhu, H. Jia, K. Wei, L. Wen, Microreactor facilitated preparation and Ni-doping of MnO_2 nanoparticles for supercapacitors. Journal of Alloys and Compounds, 889 (2021) 161772.

[3] X. Fan, L. Chen, X. Ji, T. Deng, S. Hou, J. Chen, J. Zheng, F. Wang, J. Jiang, K. Xu, C. Wang, Highly Fluorinated Interphases Enable High-Voltage Li-Metal Batteries. Chem, 4 (2018) 174-185.

[4] N. Zarshad, A.U. Rahman, J. Wu, A. Ali, F. Raziq, L. Han, P. Wang, G. Li, H. Ni, Enhanced energy density and wide potential window for K incorporated MnO_2@carbon cloth supercapacitor. Chemical Engineering Journal, 415 (2021) 128967.

[5] L. Xu, G. Pan, J. Wang, J. Li, Z. Gong, T. Lu, L. Pan, K^+ intercalated MnO_2 with ultra-long cycling life for high-performance aqueous magnesium-ion hybrid supercapacitors. Sustainable Energy & Fuels, 6 (2022) 5290-5299.

[6] L. Xu, G. Pan, C. Yu, J. Li, Z. Gong, T. Lu, L. Pan, Co-doped MnO_2 with abundant oxygen vacancies as a cathode for superior aqueous magnesium ion storage. Inorganic Chemistry Frontiers, 10 (2023) 1748-1757.

[7] H. Zhang, K. Ye, K. Zhu, R. Cang, X. Wang, G. Wang, D. Cao, Assembly of Aqueous Rechargeable Magnesium Ions Battery Capacitor: The Nanowire Mg-OMS-2/Graphene as Cathode and Activated Carbon as Anode. ACS Sustainable Chemistry & Engineering, 5 (2017) 6727-6735.

[8] S. Li, J.-G. Zhang, Y.-Y. Yan, L.-L. Yu, J.-T. Zhao, Manganese valence state regulated beta-manganese dioxide porous nanoflowers as high-performance cathodes at large current densities for aqueous magnesium ions battery capacitor. Journal of Energy Storage, 59 (2023) 106456.

[9] G. Yang, G. Qu, C. Fang, J. Deng, X. Xu, Y. Xie, T. Sun, Y. Zhu, J. Zheng, H. Zhou, An aqueous magnesium-ion hybrid supercapacitor operated at −50 °C. Green Energy & Environment, (2022) https://doi.org/10.1016/j.gee.2022.09.004.

[10] S. Alagar, S. Kumari, D. Upreti, Aashi, V. Bagchi, High-Performance Mg-Ion Supercapacitor Designed with a N-Doped Graphene Wrapped $CoMn_2O_4$ and Porous Carbon Spheres. Energy & Fuels, 36 (2022) 14442-14452.

[11] G. Qu, G. Yang, C. Fang, H. Zhou, in: 2022 IEEE International Flexible Electronics Technology Conference (IFETC), 2022, pp. 1-2.

[12] N.S. Shaikh, S.S. Mali, J.V. Patil, A.I. Mujawar, J.S. Shaikh, S.C. Pathan, S. Praserthdam, C.K. Hong, P. Kanjanaboos, Mg^{2+} ion-powered hybrid supercapacitor with β-MnO_2 as a cathode and α-Fe_2O_3 as an anode. Journal of Energy Storage, 50 (2022) 104525.

[13] X. Cao, L. Wang, J. Chen, J. Zheng, Low-Cost Aqueous Magnesium-Ion Battery Capacitor with Commercial Mn_3O_4 and Activated Carbon. ChemElectroChem, 5 (2018) 2789-2794.

[14] X. Chen, L. Han, Y. Li, G. Zhao, G. Gao, L. Yu, X. Shan, X. Xie, X. Liu, G. Zhu,

1 K-birnessite-MnO_2/hollow mulberry-like carbon complexes with stabilized and
2 superior rate performance for aqueous magnesium ion storage. Dalton Trans, 53 (2024)
3 1640-1647.
4